Mixed Source Region Signatures inside Magnetic Switchback Patches Inferred by Heavy Ion Diagnostics

Yeimy J. Rivera[1] , Samuel T. Badman[1] , Michael L. Stevens[1] , Jim M. Raines[2] , Christopher J. Owen[3] ,
Kristoff Paulson[1] , Tatiana Niembro[1] , Stefano A. Livi[2,4] , Susan T. Lepri[2] , Enrico Landi[2] , Jasper S. Halekas[5] ,
Tamar Ervin[6,7] , Ryan M. Dewey[2] , Jesse T. Coburn[3,8] , Stuart D. Bale[6,7] , and B. L. Alterman[4]

[1] Center for Astrophysics | Harvard & Smithsonian, 60 Garden Street, Cambridge, MA 02138, USA
[2] University of Michigan, Department of Climate & Space Sciences & Engineering, 2455 Hayward St. Ann Arbor, MI 48109-2143, USA
[3] Mullard Space Science Laboratory, University College London, Holmbury St. Mary, Dorking, Surrey, RH5 6NT, UK
[4] Space Science, Southwest Research Institute, 6220 Culebra Rd., San Antonio, TX, 78238, USA
[5] Department of Physics and Astronomy, University of Iowa, Iowa City, IA 52242, USA
[6] Department of Physics, University of California, Berkeley, Berkeley, CA 94720-7300, USA
[7] Space Sciences Laboratory, University of California, Berkeley, CA 94720-7450, USA
[8] Space Science Institute, Boulder, Colorado, USA

Abstract

Since Parker Solar Probe's (Parker's) first perihelion pass at the Sun, large-amplitude Alfvén waves grouped in patches have been observed near the Sun throughout the mission. Several formation processes for these magnetic switchback patches have been suggested with no definitive consensus. To provide insight into their formation, we examine the heavy ion properties of several adjacent magnetic switchback patches around Parker's 11th perihelion pass, capitalizing on a spacecraft lineup with Solar Orbiter where each samples the same solar wind streams over a large range of longitudes. Heavy ion properties (Fe/O, C^{6+}/C^{5+}, O^{7+}/O^{6+}) related to the wind's coronal origin, measured with Solar Orbiter, can be linked to switchback patch structures identified near the Sun with Parker. We find that switchback patches do not contain distinctive ion and elemental compositional signatures different from the surrounding nonswitchback solar wind. Both the patches and ambient wind exhibit a range of fast and slow wind qualities, indicating coronal sources with open and closed field lines in close proximity. These observations and modeling indicate switchback patches form in coronal hole boundary wind and with a range of source region magnetic and thermal properties. Furthermore, the heavy ion signatures suggest interchange reconnection and/or shear-driven processes may play a role in their creation.

Unified Astronomy Thesaurus concepts: Solar wind (1534); Interplanetary physics (827); Chemical abundances (224)

1. Introduction

Alfvén waves permeate interplanetary space in the form of correlated magnetic and velocity fluctuations in the solar wind (J. W. Belcher & L. J. Davis 1971). The launch of the Parker Solar Probe (Parker; N. J. Fox et al. 2016) enabled measurements of Alfvénic fluctuations to be taken closer to the corona than ever before, revealing that they assemble into well-defined large-scale structures in the near-Sun environment. The collection of large-amplitude Alfvénic fluctuations observed during Parker's perihelion passes are referred to as magnetic switchbacks (J. C. Kasper et al. 2019; S. D. Bale et al. 2019; T. D. Phan et al. 2020). Switchbacks are identified as large reversals/deflections in the magnetic field with Alfvénically correlated spikes in velocity, maintaining a near-constant magnetic field magnitude and steady electron strahl pitch-angle distribution direction. While the switchbacks are transient, lasting from a few seconds to minutes, they are grouped into "switchback patches" that span a longitude of ∼5° with similar spatial scales to supergranular cells at the photosphere (N. Fargette et al. 2021).

Switchbacks were identified during Parker's first perihelion pass (at its closest approach of $37.7 R_\odot$ or solar radii) and have been pervasive in subsequent near-Sun encounters. However, studies find that their radial evolution destroys quintessential features used to identify them near the Sun (A. Tenerani et al. 2021; G. H. H. Suen et al. 2023). Therefore, they become less and less coherent with increasing heliocentric distance.

Drivers of switchback formation are still debated, but it is suggested that they are generated in the corona or in situ in the heliosphere through a variety of mechanisms, such as interchange magnetic reconnection (Y. Yamauchi et al. 2004; G. P. Zank et al. 2020; L. A. Fisk & J. C. Kasper 2020), the expansion of the solar wind (L. Matteini et al. 2015; A. Tenerani & M. Velli 2018; J. Squire et al. 2020; M. Shoda et al. 2021), coronal jets (A. C. Sterling & R. L. Moore 2020), and velocity shear and footpoint motion (S. Landi et al. 2006; C. Shi et al. 2020; D. Ruffolo et al. 2020; N. A. Schwadron & D. J. McComas 2021). Their compositional properties play a major role to track them back to their source region (J. C. Kasper et al. 2007; J. Huang et al. 2023). For instance, S. D. Bale et al. (2021) noticed increases of the alpha-to-proton abundance within patches of switchbacks interpreted as a consequence of magnetic reconnection processes, in contrast to M. D. McManus et al. (2022), who found no consistent composition signatures after analyzing around 100 switchback events during the third and fourth Parker encounters.

Heavy ion measurements connected to switchbacks can provide diagnostics of coronal source region properties that can be used to disambiguate their source, a linkage that has not previously been made (Y. Rivera et al. 2022). While Parker does not measure heavy ions ($Z > 2$, where Z is the atomic number or number of protons) for this type of analysis, Solar Orbiter (D. Müller et al. 2020) carries a heavy ion resolving mass spectrometer, the Heavy Ion Sensor (HIS; S. Livi et al. 2023), as part of the Solar Wind Analyzer (SWA; C. J. Owen et al. 2020) suite that can sample the ion and elemental composition, albeit at larger heliocentric distances (closest distance at $\sim 60\,R_\odot$) where switchback signatures are more ambiguous. However, this ambiguity can be mitigated through well-aligned spacecraft configurations, where observations of solar wind containing switchbacks taken by Parker closer to the Sun can be later sampled by Solar Orbiter to examine their heavy ion composition.

The ionization states of heavy ions measured in the solar wind preserve signatures of the electron temperature and density of the corona they traveled through, making them excellent probes of the solar wind's source region characteristics. Ion abundances measured in situ throughout the heliosphere are governed by ionization and recombination processes happening in the corona and during the initial stages of outflow (E. Landi et al. 2012; B. Boe et al. 2018; C. R. Gilly & S. R. Cranmer 2020). Ionization and recombination of ions in the plasma are determined by the plasma's electron temperature and density and bulk flow. As collisions in the plasma are reduced due to expansion with increasing distance from the Sun, the ionization and recombination processes become less and less effective. Eventually ions convected in the solar wind reach their freeze-in distance or heliocentric location where their relative abundances no longer change. In the solar wind, carbon and oxygen ions freeze in closer to the Sun ($1–1.5\,R_\odot$), while iron ions can continue to ionize and recombine up to $3–5\,R_\odot$ (E. Landi et al. 2012). Therefore, while other solar wind properties can change at different radial distances, heavy ion relative abundances are nearly static once the solar wind escapes the low and middle corona (M. J. West et al. 2023 and references therein).

Elemental abundances in the solar wind are modulated by their source region's magnetic topology at the Sun. Decades of observations of elemental abundances derived from remote and in situ observations indicate strong first ionization potential (FIP)-related fractionation in closed field regions of the Sun and associated slow-speed wind (S. R. Pottasch 1963; J. Geiss et al. 1995; J. C. Raymond et al. 1997; R. von Steiger et al. 2000; U. Feldman & J. M. Laming 2000). The FIP effect is the observed enhancement relative to photospheric composition of elemental abundances for atoms with an ionization energy below ~ 10 eV, while elements above this threshold are either not affected or even depleted. The leading model that explains the FIP effect is connected to Alfvén waves reflecting/refracting across the chromospheric-to-coronal boundary, giving rise to the ponderomotive force. Depending on where Alfvén waves are reflected, the ponderomotive force will then act to preferentially transport charged low-to-mid-FIP elements (e.g., sulfur and carbon that sit at the low- and high-FIP energy threshold) into the corona (J. M. Laming 2004, 2012; J. M. Laming et al. 2019). Once the solar wind is formed, elemental abundances remain fixed in the outflowing solar wind stream, maintaining the properties of its coronal source.

The elemental abundances connected through remote and in situ observations have been important for identifying the sources of slow solar wind (D. H. Brooks et al. 2015) and connecting transient structures from the Sun to the heliosphere (S. Parenti et al. 2021).

As indicated above, we can connect heavy ion properties measured by Solar Orbiter to Parker during periods where they each measure the same solar wind streams. As such, we use a spacecraft conjunction between Parker's 11th perihelion pass (0.06 au) and Solar Orbiter near the Sun–Earth line at 0.6 au to connect heavy ion observations taken at Solar Orbiter to several subsequent switchback patches identified closer to the Sun with Parker. The Parker–Solar Orbiter conjunction has been examined in several cases (T. Ervin et al. 2024; Y. J. Rivera et al. 2024). It is a special alignment, as both spacecraft cover similar Carrington longitudes and latitudes, which is rare. T. Ervin et al. (2024) examine the heavy ion composition at Solar Orbiter to map the distinctive solar sources of several fast and slow Alfvénic wind streams observed across an alignment in longitude spanning $\sim 150°$. The work indicated that the fast wind and Alfvénic slow wind in this encounter originated from coronal holes and their boundaries, respectively. Y. J. Rivera et al. (2024) examine the radial evolution of a switchback patch during the alignment included in this study, finding their contribution to be significant and necessary to the full description of the heating and acceleration experienced by the fast solar wind. Y. J. Rivera et al. (2024) analyze the elemental and ion composition of the switchback patch, finding its Fe/O abundance ratio to be in line with fast solar wind elemental composition, albeit indicating some low-FIP enhancement.

In this work, we expand on the analysis from Y. J. Rivera et al. (2024) to examine the ion and elemental composition of adjacent switchback patches observed with Parker and eventually measured at Solar Orbiter. Through ballistic back-mapping methods used previously (T. Ervin et al. 2024; Y. J. Rivera et al. 2024), we align switchback patch observations at Parker to O^{7+}/O^{6+}, C^{6+}/C^{5+}, and Fe/O measurements connected to the same mapped source surface longitude. We find that heavy ion measurements show variation across neighboring patches in both ion and elemental composition, indicating changes associated with source region conditions and locations at the Sun. The Fe/O variability and electron temperature connected to the patches span between typical coronal hole and quiet Sun properties (in contrast to active regions at the Sun, which exhibit a much more extreme FIP bias), indicating a source with a mixture of open/closed magnetic field topology, such as coronal hole boundaries.

The paper is organized as follows: Section 2 describes the observations from Parker and Solar Orbiter and the ballistic mapping technique. Section 3 presents the heavy ion measurements characteristics within the switchback patches observed at Parker. Section 4 summarizes the results.

2. Stream Matching

2.1. Parker and Solar Orbiter Observations

At Parker, we examine observations from the SPAN-Ai instrument to compute the bulk solar wind velocities (R. Livi et al. 2022). SPAN-Ai couples an electrostatic analyzer and time-of-flight (TOF) component to resolve the incident angle, mass per charge, and energy per charge of incoming ions. The mass discrimination made possible by the TOF analyzer allows
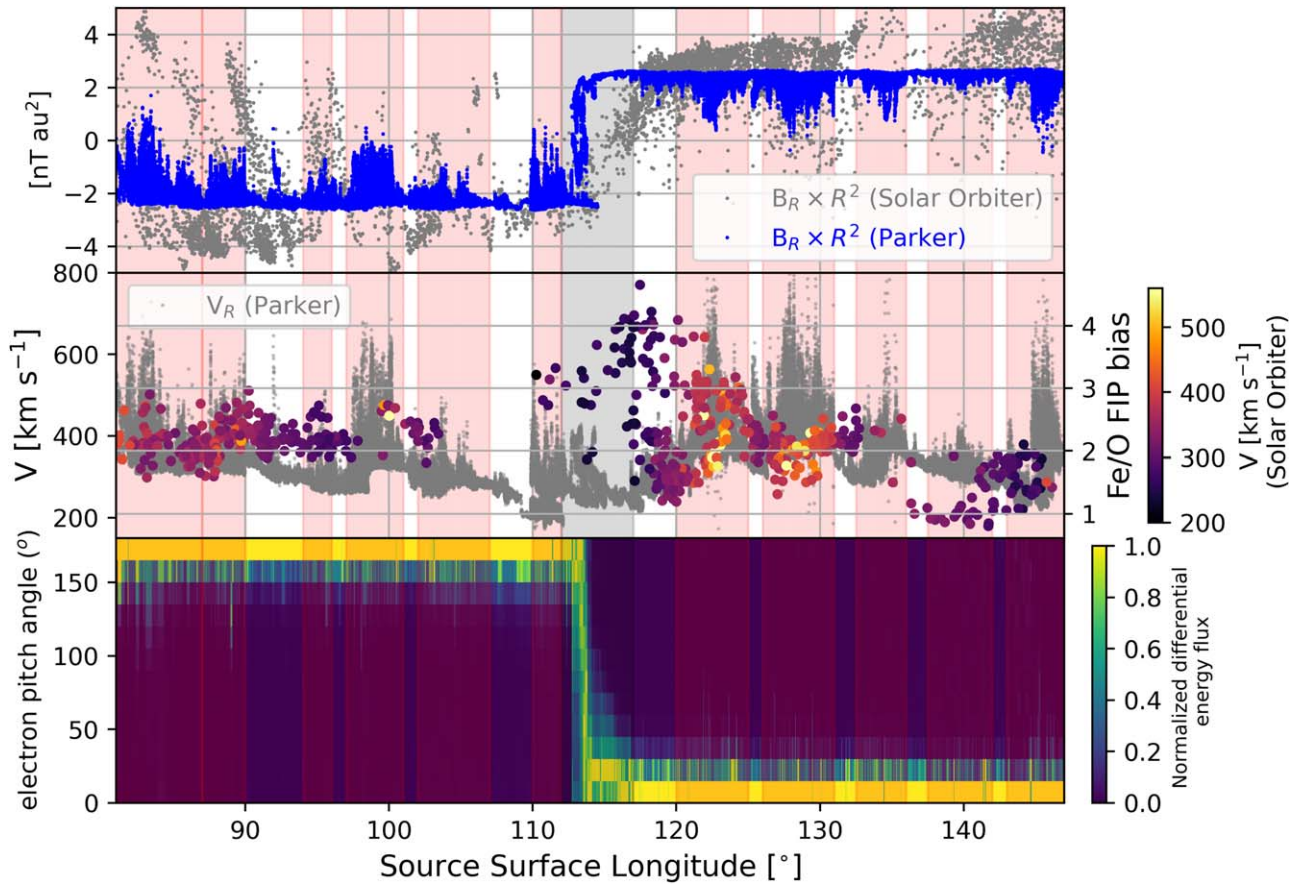
Figure 1. Multipanel plot showing the switchback properties at Parker and compositional properties at Solar Orbiter across source surface longitude. Top: radial magnetic field B_R multiplied by heliocentric distance squared for Parker (blue) and Solar Orbiter (gray). Middle: the left vertical axis shows the radial speed at Parker (gray), and the right axis shows the Fe/O ratio normalized to the Sun's photospheric abundance as FIP bias. The FIP bias is colored by the wind speed at Solar Orbiter. Bottom: normalized differential energy flux of 432.69 eV electrons measured at Parker. Shaded red regions identify individual switchback patches characterized by the speed, magnetic field, and electron e-PAD signatures. The shaded gray region is the current sheet crossing.

for the identification of separate ions species in the solar wind, mainly the most abundant species—proton and alpha particles or He^{2+}. We include electron measurements from SPAN-e (P. L. Whittlesey et al. 2020), where the electron temperature is derived by methods described in J. S. Halekas et al. 2020. Additionally, the 3D magnetic field components are measured by the fluxgate magnetometer (MAG) on FIELDS at 4 vectors/ cyc that captures the rapid changes in the magnetic field (S. D. Bale et al. 2016).

At Solar Orbiter, measurements of the magnetic field are taken by another MAG at 8 vectors s^{-1} (T. S. Horbury et al. 2020). Observations of protons, alpha particles, and heavier ions across this period were taken by Proton-Alpha System (PAS) and HIS, which are part of the SWA suite (C. J. Owen et al. 2020). The proton velocities were measured with the PAS instrument with 4 s full-scan 3D particle distributions. Observations of the heavier ions ($Z > 2$) were measured at a 30 s cadence and accumulated to 10 minute resolution using the TOF mass spectrometer on HIS (S. Livi et al. 2023).

2.2. Ballistic Mapping

As in T. Ervin et al. (2024) and Y. J. Rivera et al. (2024), Solar Orbiter and Parker measurements are cast from time series to spatial coordinates termed "source surface longitude" by using ballistic mapping (J. T. Nolte & E. C. Roelof 1973; D. Stansby et al. 2019; S. T. Badman et al. 2020) to associate

each measurement with a heliographic location at the edge of the corona at $2.5R_\odot$. This process models plasma parcel streamlines as Archimedean spirals in the solar corotating frame using the measured solar wind velocity at each spacecraft and assuming the parcel moves at a constant radial speed. In comparison to models that account for coronal corotation and acceleration, this approximation has recently been quantified to yield results with errors under $5°$ when starting from 1 au and monotonically decreasing with close approach to the Sun (J. B. Dakeyo et al. 2024). Here, our measurements are taken at 0.6 au (Solar Orbiter) and 0.063 au (Parker) and so are expected to be even smaller. We study statistically a region of source surface longitude of $70°$ in width and identify switchback patches of a similar width or greater than $5°$.

3. Heavy Ion Observations

3.1. Elemental Composition

Figure 1 shows a three-panel plot of the properties of Parker and Solar Orbiter ballistically backmapped across source surface longitude. The top panel shows the magnetic field radial component multiplied by the radial distance squared at each spacecraft for Solar Orbiter (gray) and Parker (blue) in order to account for the radial dependence in the radial component of the magnetic field between the two spacecraft. The middle panel shows the radial speed at Parker (gray) along with the Fe/O FIP bias colored by the bulk speed at Solar

Orbiter. The Fe/O FIP bias is computed by normalizing the relative elemental abundances of Fe and O to their photospheric elemental composition from M. Asplund et al. (2021). A FIP bias above 1 indicates some enhancement of Fe or depletion of O in the plasma and is interpreted as indicating the plasma has spent time on closed magnetic loops prior to escaping. The bottom panel shows the column normalized electron pitch-angle distribution (e-PAD) of suprathermal electrons across $0–180°$ in the energy range 432.69 eV. The red shaded regions denote the individual, coherent switchback patches across source surface longitude $81°–147°$ spanning the full day of 2022 February 25 at Parker and spanning 2022 February 23 to March 4 at Solar Orbiter. The switchback patches were identified through their typical characteristics at Parker (N. Fargette et al. 2021; S. D. Bale et al. 2021):

1. large fluctuations of radial magnetic field component correlated to fluctuations in speed;
2. constant magnetic field magnitude across the patch structure;
3. steady field-aligned electron beam;
4. consistent longitudinal width around $5°$.

A current sheet crossing occurs midway through Parker's closest approach, showing a change in the magnetic field polarity inferred from the e-PAD and a local speed minimum near $113°$. The current sheet crossing is also observed at Solar Orbiter, as indicated by the change in the radial magnetic field components also near $113°–117°$. The well-aligned current sheet crossings at both spacecraft demonstrates an accurate mapping of flows between Parker (at $\sim13.5\,R_\odot$) and Solar Orbiter (at $\sim130\,R_\odot$) near the current sheet. Therefore, we focus on characterizing switchback patches embedded in solar wind within $\sim30°$ of the current sheet crossing where we have the greatest confidence that Parker and Solar Orbiter sampled the same streams.

As shown in the middle panel of Figure 1, we find that the Fe/O FIP bias is generally observed to be between 2 and 3 within the switchback patches spanning this longitude range, with the exception of the small amplitude patch near $137°–142°$ with a photospheric elemental composition near 1. Generally, the variability of the Fe/O FIP bias measured across wind speed and the solar cycle spans 1.7 ± 1.1 (slow) to 0.8 ± 0.44 (fast) in solar max and 1.4 ± 1.1 (slow) to 0.9 ± 0.34 (fast) in solar minimum conditions (S. T. Lepri et al. 2013). Therefore, the mean values observed are closer to what is expected for slow solar wind, for solar max or minimum. However, the large variability within the observed patches covers a mixture of photospheric to coronal abundances connected to both open and closed field structures at the Sun.

3.2. Electron Temperature and Ion Abundances

Figure 2 shows the ion ratios and the associated freeze-in temperature across the same source surface longitude as Figure 1. The top plot shows the ballistically backmapped relative abundance ion ratios of O^{7+}/O^{6+} and C^{6+}/C^{5+} at Solar Orbiter. The bottom plot shows the freeze-in temperature, $T_\text{freeze-in}$, derived from the ion formation temperatures, colored by the bulk speed at Solar Orbiter, under the assumption of ionization equilibrium conditions, as well as the computed electron temperature at Parker (black). The shaded regions are the same switchback patches identified from properties in Figure 1, and the shaded black region shows the current sheet

crossing location. The $T_\text{freeze-in}$ is derived by computing the ratio of the relative abundances of each ion as a function of electron temperature using CHIANTI v.10, detailed in G. Del Zanna et al. (2021). $T_\text{freeze-in}$ is the temperature where the computed curve of the ion ratio matches the ion ratio measured in situ. The accuracy of the derived freeze-in temperature from each ion ratio relative to a meaningful coronal temperatures relies on the ions freezing in while in ionization equilibrium. Therefore we do not claim in each case that the temperature is definitively reflective of the source region at a specific place in the corona.

Generally, the ion ratios in the top panel of Figure 2 show profiles that increase nearly symmetrically as they approach the current sheet (near $115°$), with their highest values within the current sheet as typically observed (Y. J. Rivera et al. 2021; B. J. Lynch et al. 2023). The associated freeze-in temperatures derived from both ratios show correlated behavior and a similar profile to the electron temperature measured independently in situ at Parker (black). We compute a correlation coefficient (ratio of the covariance of the two time series divided by the standard deviation of each time series multiplied together) between the ion parameters and the electron temperature at Parker to quantify their correlated behavior. We downsample each series into $2°$ averaged longitudinal bins for comparison. We find the correlation coefficient of electron temperature at Parker and $T_\text{freeze-in}$ from O^{7+}/O^{6+} to be 0.87, while the electron temperature at Parker and the O^{7+}/O^{6+} ion ratio shows an even higher correlated value of 0.93. Similarly for the carbon ratios, we find the correlation coefficient of the electron temperature at Parker and $T_\text{freeze-in}$ from C^{6+}/C^{5+} is 0.80, while the electron temperature at Parker and the C^{6+}/C^{5+} ion ratio is 0.87. We also compute the correlation coefficient of O^{7+}/O^{6+} and C^{6+}/C^{5+} that returns a similar correlation coefficient of 0.91, showing a strong correlated behavior overall.

The freeze-in temperature derived from oxygen charge states shows a systematic $0.2\,\text{MK}$ difference across the entire range relative to that derived from carbon. The changes in the freeze-in temperature would be consistent with a difference in freeze-in radial distances between the carbon and oxygen ratios (E. Landi et al. 2012). However, some deviation from ionization equilibrium cannot be ruled out as responsible for the shift.

Overall, the ion ratios are less structured compared to the Fe/O FIP bias and show small variation in both the freeze-in and local electron temperature across the switchback patches. The electron temperature measured at Parker and the ion ratios/freeze-in temperatures show similar substructure. In particular, we find correlated changes in the electron temperature profile at Parker and ion ratios across several switchback boundaries. For instance, all three profiles show a steady profile between source surface longitudes $87°$ and $94°$, with a steady rise in temperature after that point. We also observe a concurrent increase in temperature near $131°$, likely associated with a change in source region properties across solar wind streams. All profiles indicate a steady electron temperature across two switchback patches spanning $137°–147°$.

We find larger variation in electron temperatures across longitude patches than within individual patches. The left plot of Figure 3 shows the mean in situ electron temperature from Parker across individual switchback patches (red), in between the switchback periods (blue), and spanning the current sheet
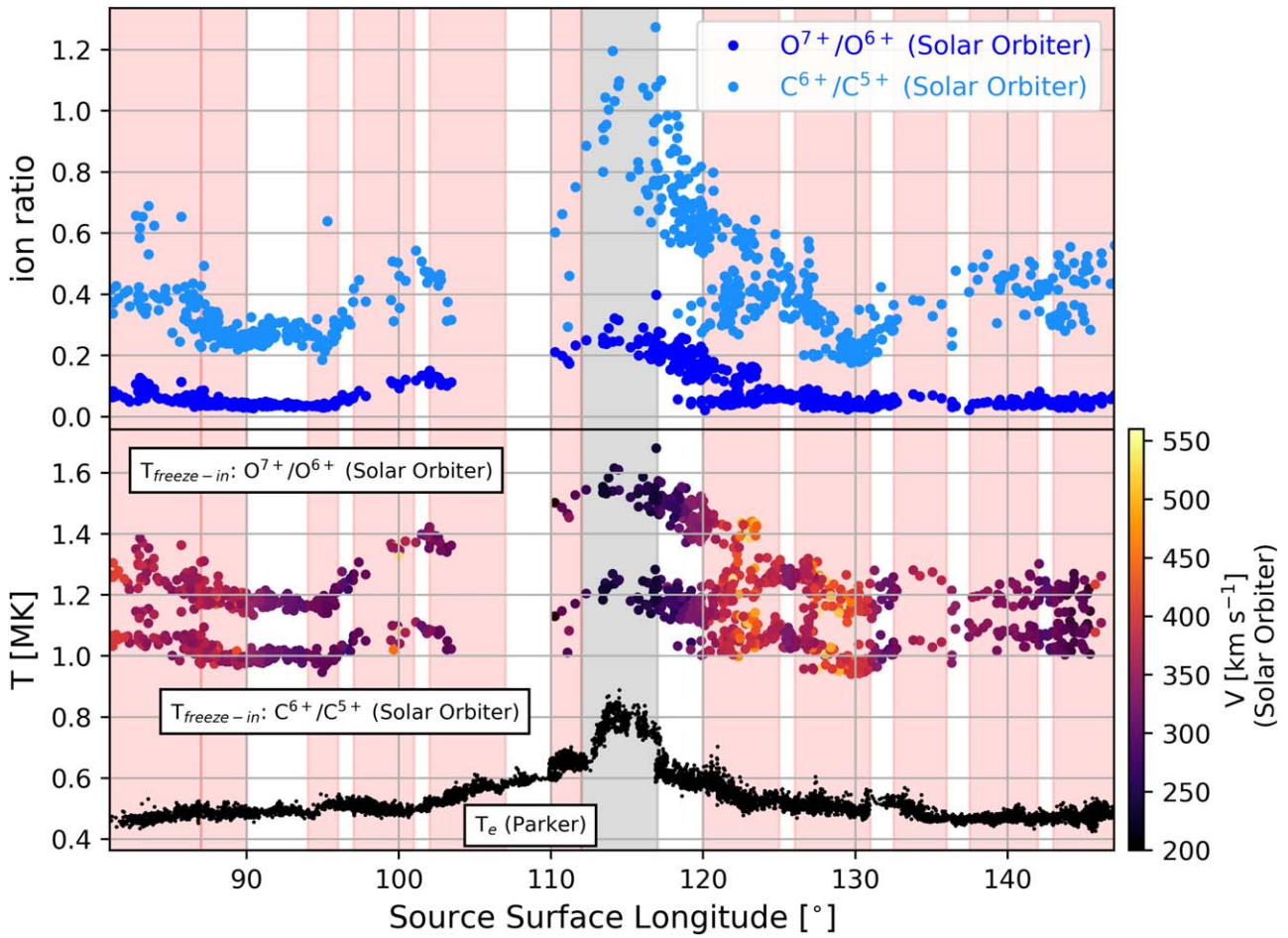
Figure 2. Two-panel plot showing the ion ratio and associated electron temperature properties of the solar wind. Top: relative abundance ratio of O^{7+}/O^{6+} and C^{6+}/C^{5+} measured at Solar Orbiter. Bottom: derived electron temperature from O^{7+}/O^{6+} and C^{6+}/C^{5+} formation temperatures from Solar Orbiter and electron temperature computed in situ at Parker. Shaded regions are the same as Figure 1.
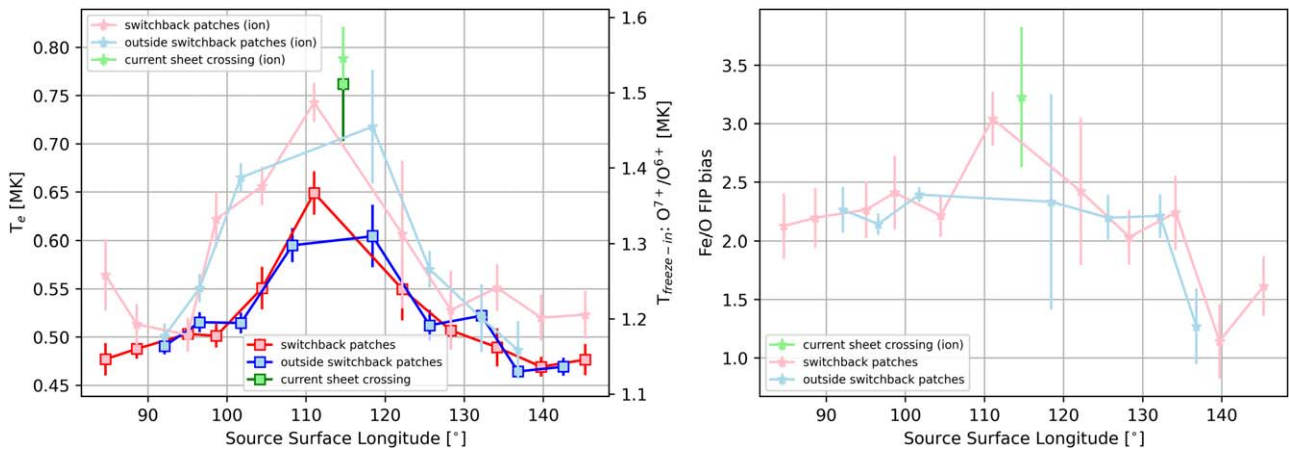
Figure 3. The left plot shows the mean electron temperature computed within (red) and outside (blue) switchback patches and at the current sheet (green) with the standard deviation across the longitude range. The electron temperature computed at Parker is shown in the solid lines associated with the left vertical axis and the ion ratio–derived freeze-in temperature in the light colors associated with the right vertical axis. The plot on the right shows the mean and standard deviation of the Fe/O FIP bias for the different cases.

(green) with the lighter colors showing the same classification except for the freeze-in temperature derived from O^{7+}/O^{6+}. The vertical bars in the plot are the standard deviation of the temperature within the different longitude patches and indicate the variability of the temperature within that region. The figure shows that at Parker, the typical standard deviation within individual patches (a single red box) is much smaller (on average $\sim$0.018 MK) compared to the variation in the electron temperature of all the patches across longitude (variation across all red boxes in Figure 3), with a standard deviation $\sim$0.05 MK.

The same is observed in the freeze-in temperature. We note that the period covered by the Parker measurements spans a radial distance of $2.6 R_\odot$ between 13.28 and $15.9 R_\odot$, which is too small (J.-B. Dakeyo et al. 2022) to explain the variation seen in the in situ electron temperature in Figure 3. Therefore, we attribute the variation in the in situ electron temperature at Parker to changes in the source region conditions rather than radial evolution.

We find Fe/O FIP bias shows large variability across different patches, as shown in the pink curve of the right plot in Figure 3. The vertical bars are computed in the same manner as the left plot. However, the FIP bias is similar to outside of the switchback patches, suggesting their source is similar to the surrounding nonswitchback solar wind.

4. Summary and Conclusions

We examine the heavy ion composition of several adjacent switchback patches measured during Parker's 11th perihelion pass centered on 2022 February 25. Encounter 11 occurred during a well-aligned conjunction with Solar Orbiter that sampled a similar longitude and latitude as Parker. The spacecraft conjunction enabled young solar wind measured in situ by Parker (at $13.5 R_\odot$) to be connected to solar wind streams measured at Solar Orbiter (at $130 R_\odot$). Through ballistic backmapping from both spacecraft to the source surface at $2.5 R_\odot$, the properties at Parker were aligned in longitude to measurements at Solar Orbiter. We used a current sheet crossing as an indication of backmapping accuracy that served as an anchor point to compare the surrounding solar wind streams. We mapped switchback structures observed at Parker to measurements of heavy ions observed at Solar Orbiter to determine the Fe/O abundance and electron temperature properties within each patch. Given Parker's proximity to the Sun, switchback patches appear more coherent, making them more easily identifiable than at larger distances where they are less well organized. However, Parker does not measure the needed heavy ion signatures. Therefore, the alignment and use of both spacecraft were crucial to mapping their heavy ion properties.

We find the elemental composition (Fe/O) and the ion ratios suggest some variability in the solar source of the neighboring switchback patches. The Fe/O FIP bias across the adjacent patches shows a range between 1 and 3, suggesting their source is undergoing the FIP effect to varying degrees. However, the strong variability between and within each switchback patch suggests distinct sources, or some combination of coronal regions, are related to the individual patches.

Similarly, but to a lesser extent, the ion ratios indicate some substructure across adjacent patches. The derived freeze-in temperatures from the carbon and oxygen ratios maintain a similar profile to the ion ratios themselves as well as to the in situ electron temperature measured by Parker. The strong correlation in features observed between ion ratios and the ion ratio–derived coronal electron temperature from Solar Orbiter observations and in situ electron temperature measured independently at Parker indicate (1) a compelling connection between solar wind observations at Parker and Solar Orbiter, (2) changing source conditions across adjacent patches, and (3) cooler electron temperature (in situ) compared to current sheet plasma.

We conclude that heavy ion measurements show notable variation across neighboring patches in both ion and elemental composition. The elemental composition indicates the Fe/O FIP bias spans between typical coronal hole and quiet Sun composition, suggesting both as their source (G. Del Zanna 2019) in contrast to active regions that contain the most extreme low-FIP enhancements (FIP bias > 4) and the hottest coronal plasma at 3–10 MK (T. Yoshida & S. Tsuneta 1996; U. Feldman & J. M. Laming 2000; K. G. Widing & U. Feldman 2001; F. Reale 2010). We note we do not see examples of switchback patches forming in wind with composition properties of current sheet plasma, active region outflow, or pristine fast wind. The range of Fe/O FIP bias measured within and across switchback patches indicates their solar source is a combination of open (not low-FIP-enhanced) and closed (low-FIP-enhanced) field structures. This result, along with modeling in T. Ervin et al. (2024) and Y. J. Rivera et al. (2024) throughout this timeframe, connects the switchback patches to open/closed field boundaries at the edge of coronal hole where a transition of photospheric to low-FIP-enhanced Fe/O values is observed (F. Xu & J. E. Borovsky 2015; M. Stakhiv et al. 2015). Extended equatorial coronal holes were a predominant feature on disk during this time interval in line with the switchback patches mapping to open/close field regions (T. Ervin et al. 2024; Y. J. Rivera et al. 2024). The range of compositional values indicates a diversity of source thermal and magnetic conditions within this distinct source type, all of which enable the formation of switchback patches.

We note that because the main coronal features associated with the switchback patches examined in this study were mapped to extended coronal holes, it is difficult to distinguish from this interval if switchback patches are simply reflecting the compositional characteristics of the background solar wind they are embedded in or if they require the observed source region properties seen in this study. Future work should identify similar aligned observations with more clear extremes in source region properties, such as those with large equatorial coronal holes, to verify if switchback patches in these cases diverge from background solar wind compositional signatures.

4.1. Switchback Formation Processes

As listed in the introduction, there are several switchback formation processes theorized. Here we compare the predicted observables from some of these processes to the heavy ion and electron temperature characteristics of switchback patches we find in this study, which were as follows:

1. Open and closed field FIP bias characteristics.
2. Steady ion abundances congruent with nonswitchback solar wind.
3. Steady electron temperature similar to nonswitchback solar wind temperature.

The solar wind bearing the switchback patches in this interval has been mapped to open/closed boundaries (T. Ervin et al. 2024) that are ideal locations for interchange reconnection to occur, a phenomenon featured in many theories of switchback formation (L. A. Fisk & J. C. Kasper 2020; S. D. Bale et al. 2023). However, the lack of evidence for strongly enhanced electron temperatures from Parker (above surrounding solar wind conditions) suggests any strong heating occurring in such reconnection is either averaged out across the stream long before the plasma reaches Parker or happening above the ion's freeze-in height such that the ions do not reflect the heating (R. B. Scott et al. 2022).

Similarly, velocity shear-driven formation processes would be in line with a mixed FIP bias observation since it requires adjacent fast and slow solar wind to drive switchback formation (C. Shi et al. 2020; D. Ruffolo et al. 2020; N. A. Schwadron & D. J. McComas 2021). However, this formation process would also ultimately map to regions of open/closed field such as coronal hole boundaries, as in the interchange reconnection case, where slow and fast solar wind form in close proximity. For cases of similar source regions, composition measurements do not immediately distinguish these two processes.

Lastly, coronal jets would indicate the switchbacks form through the ejection of minifilament flux ropes (A. C. Sterling & R. L. Moore 2020). However, similar to larger-scale flux ropes, this would be indicated through enhancements to the ion abundances and Fe/O FIP bias that would result in a higher mean value compared to background solar wind properties, but that is not observed in this interval.

ORCID iDs

Yeimy J. Rivera https://orcid.org/0000-0002-8748-2123
Samuel T. Badman https://orcid.org/0000-0002-6145-436X
Michael L. Stevens https://orcid.org/0000-0002-7728-0085
Jim M. Raines https://orcid.org/0000-0001-5956-9523
Christopher J. Owen https://orcid.org/0000-0002-5982-4667
Kristoff Paulson https://orcid.org/0000-0002-5699-090X
Tatiana Niembro https://orcid.org/0000-0001-6692-9187
Stefano A. Livi https://orcid.org/0000-0002-4149-7311
Susan T. Lepri https://orcid.org/0000-0003-1611-227X
Enrico Landi https://orcid.org/0000-0002-9325-9884
Jasper S. Halekas https://orcid.org/0000-0001-5258-6128
Tamar Ervin https://orcid.org/0000-0002-8475-8606
Ryan M. Dewey https://orcid.org/0000-0003-4437-0698
Jesse T. Coburn https://orcid.org/0000-0002-2576-0992
Stuart D. Bale https://orcid.org/0000-0002-1989-3596
B. L. Alterman https://orcid.org/0000-0001-6673-3432

References

Asplund, M., Amarsi, A. M., & Grevesse, N. 2021, A&A, 653, A141
Badman, S. T., Bale, S. D., Martínez Oliveros, J. C., et al. 2020, ApJS, 246, 23
Bale, S. D., Goetz, K., Harvey, P. R., et al. 2016, SSRv, 204, 49
Bale, S. D., Badman, S. T., Bonnell, J. W., et al. 2019, Natur, 576, 237
Bale, S. D., Horbury, T. S., Velli, M., et al. 2021, ApJ, 923, 174
Bale, S. D., Drake, J. F., McManus, M. D., et al. 2023, Natur, 618, 252
Belcher, J. W., & Davis, L. J. 1971, JGR, 76, 3534
Boe, B., Habbal, S., Druckmüller, M., et al. 2018, ApJ, 859, 155
Brooks, D. H., Ugarte-Urra, I., & Warren, H. P. 2015, NatCo, 6, 5947
Dakeyo, J. B., Badman, S. T., Rouillard, A. P., et al. 2024, A&A, 686, A12
Dakeyo, J.-B., Maksimovic, M., Démoulin, P., Halekas, J., & Stevens, M. L. 2022, ApJ, 940, 130
Del Zanna, G. 2019, A&A, 624, A36
Del Zanna, G., Dere, K. P., Young, P. R., & Landi, E. 2021, ApJ, 909, 38
Ervin, T., Bale, S. D., Badman, S. T., et al. 2024, ApJ, 969, 83
Fargette, N., Lavraud, B., Rouillard, A. P., et al. 2021, ApJ, 919, 96
Feldman, U., & Laming, J. M. 2000, PhyS, 61, 222
Fisk, L. A., & Kasper, J. C. 2020, ApJL, 894, L4
Fox, N. J., Velli, M. C., Bale, S. D., et al. 2016, SSRv, 204, 7
Geiss, J., Gloeckler, G., & von Steiger, R. 1995, SSRv, 72, 49
Gilly, C. R., & Cranmer, S. R. 2020, ApJ, 901, 150
Halekas, J. S., Whittlesey, P., Larson, D. E., et al. 2020, ApJS, 246, 22
Horbury, T. S., O'Brien, H., Carrasco Blazquez, I., et al. 2020, A&A, 642, A9
Huang, J., Kasper, J. C., Fisk, L. A., et al. 2023, ApJ, 952, 33
Kasper, J. C., Stevens, M. L., Lazarus, A. J., Steinberg, J. T., & Ogilvie, K. W. 2007, ApJ, 660, 901
Kasper, J. C., Bale, S. D., Belcher, J. W., et al. 2019, Natur, 576, 228
Laming, J. M. 2004, ApJ, 614, 1063
Laming, J. M. 2012, ApJ, 744, 115
Laming, J. M., Vourlidas, A., Korendyke, C., et al. 2019, ApJ, 879, 124
Landi, E., Gruesbeck, J. R., Lepri, S. T., & Zurbuchen, T. H. 2012, ApJ, 750, 159
Landi, S., Hellinger, P., & Velli, M. 2006, GeoRL, 33, L14101
Lepri, S. T., Landi, E., & Zurbuchen, T. H. 2013, ApJ, 768, 94
Livi, R., Larson, D. E., Kasper, J. C., et al. 2022, ApJ, 938, 138
Livi, S., Lepri, S. T., Raines, J. M., et al. 2023, A&A, 676, A36
Lynch, B. J., Viall, N. M., Higginson, A. K., et al. 2023, ApJ, 949, 14
Matteini, L., Horbury, T. S., Pantellini, F., Velli, M., & Schwartz, S. J. 2015, ApJ, 802, 11
McManus, M. D., Verniero, J., Bale, S. D., et al. 2022, ApJ, 933, 43
Müller, D., Cyr, O. C., St., Zouganelis, I., et al. 2020, A&A, 642, A1
Nolte, J. T., & Roelof, E. C. 1973, SoPh, 33, 241
Owen, C. J., Bruno, R., Livi, S., et al. 2020, A&A, 642, A16
Parenti, S., Chifu, I., Del Zanna, G., et al. 2021, SSRv, 217, 78
Phan, T. D., Bale, S. D., Eastwood, J. P., et al. 2020, ApJS, 246, 34
Pottasch, S. R. 1963, ApJ, 137, 945
Raymond, J. C., Kohl, J. L., Noci, G., et al. 1997, SoPh, 175, 645
Reale, F. 2010, LRSP, 7, 5
Rivera, Y. J., Badman, S. T., & Stevens, M. L. 2024, Sci, 385, 962
Rivera, Y. J., Lepri, S. T., Raymond, J. C., et al. 2021, ApJ, 921, 93
Rivera, Y., Higginson, A., Lepri, S. T., et al. 2022, FrASS, 9, 417
Ruffolo, D., Matthaeus, W. H., Chhiber, R., et al. 2020, ApJ, 902, 94
Schwadron, N. A., & McComas, D. J. 2021, ApJ, 909, 95
Scott, R. B., Bradshaw, S. J., & Linton, M. G. 2022, ApJ, 933, 72
Shi, C., Velli, M., Tenerani, A., Rappazzo, F., & Réville, V. 2020, ApJ, 888, 68
Shoda, M., Chandran, B. D. G., & Cranmer, S. R. 2021, ApJ, 915, 52
Squire, J., Chandran, B. D. G., & Meyrand, R. 2020, ApJL, 891, L2
Stakhiv, M., Landi, E., Lepri, S. T., Oran, R., & Zurbuchen, T. H. 2015, ApJ, 801, 100
Stansby, D., Horbury, T. S., Wallace, S., & Arge, C. N. 2019, RNAAS, 3, 57
Sterling, A. C., & Moore, R. L. 2020, ApJL, 896, L18
Suen, G. H. H., Owen, C. J., Verscharen, D., et al. 2023, A&A, 675, A128
Tenerani, A., Sioulas, N., Matteini, L., et al. 2021, ApJL, 919, L31
Tenerani, A., & Velli, M. 2018, ApJL, 867, L26
von Steiger, R., Schwadron, N. A., Fisk, L. A., et al. 2000, JGR, 105, 27217
West, M. J., Seaton, D. B., Wexler, D. B., et al. 2023, SoPh, 298, 78
Whittlesey, P. L., Larson, D. E., Kasper, J. C., et al. 2020, ApJS, 246, 74
Widing, K. G., & Feldman, U. 2001, ApJ, 555, 426
Xu, F., & Borovsky, J. E. 2015, JGRA, 120, 70
Yamauchi, Y., Suess, S. T., Steinberg, J. T., & Sakurai, T. 2004, JGRA, 109, A03104
Yoshida, T., & Tsuneta, S. 1996, ApJ, 459, 342
Zank, G. P., Nakanotani, M., Zhao, L. L., Adhikari, L., & Kasper, J. 2020, ApJ, 903, 1